Aalborg Universitet

AALBORG UNIVERSITY

Torque ripple minimization of a five-phase induction motor under open-phase faults using symmetrical components

He, Shan; Sui, Xin; Liu, Zijian; Kang, Min; Zhou, Dao; Blaabjerg, Frede

[Link to publication from Aalborg University](#)

Torque Ripple Minimization of a Five-Phase Induction Motor Under Open-Phase Faults Using Symmetrical Components

SHAN HE[1], (Graduate Student Member, IEEE),
XIN SUI[1], (Graduate Student Member, IEEE), **ZIJIAN LIU**[2], **MIN KANG**[3],
DAO ZHOU[1], (Senior Member, IEEE), AND **FREDE BLAABJERG**[1], (Fellow, IEEE)
[1]Department of Energy Technology, Aalborg University, 9220 Aalborg, Denmark
[2]Department of Electrical Engineering, Tsinghua University, Beijing 100084, China
[3]College of Electrical Engineering, Zhejiang University of Science and Technology, Hangzhou 310023, China

Corresponding author: Frede Blaabjerg (fbl@et.aau.dk)

ABSTRACT In order to minimize the torque ripple of five-phase induction motor under open-phase faults, the conventional strategy makes the stator current space vectors to move along the circular anticlockwise trajectories. However, the torque ripple is suppressed indirectly based on the coupling between spatial harmonic fields, and the analytical expression of the torque ripple is not considered. In this paper, according to the steady-state model using symmetrical components (SCs), the torque ripple is mainly caused by the first and fourth SCs. Hence, several possible current commands are deduced under single-phase fault and two-phase fault by suppressing the first and fourth SCs. Under single-phase fault, the proposed strategy shows better performance than the conventional strategy in terms of torque ripple, average torque and efficiency. Under adjacent two-phase fault, the proposed strategy shows lower torque ripple but a lower efficiency than the conventional strategy, and these two strategies can be selected according to the specific application requirements. Finally, the effectiveness of the proposed strategy is validated by the experimental results.

INDEX TERMS Five-phase induction motor, fault-tolerant operation, minimum torque ripple, symmetrical component.

NOMENCLATURE

L_{mk}	magnetic inductance with sequence order k
l_{0sk} and l_{0rk}	stator and rotor leakage inductance with sequence order k
R_s	stator resistance
R_{rk}	rotor resistance with sequence order k
ω	fundamental synchronous electric angular speed
ω_r	rotor mechanical angular speed
ω_{s1}	fundamental slip angular speed
ω_{nk}	synchronous electric angular speed with harmonic order n and sequence order k
$\omega_{c(max)}$	maximum cross frequency
I_{mn}	RMS current with harmonic order n in the healthy case
MT	synchronous frame whose T-axis is 90° leading to M-axis
i_{Ms1}^* and i_{Ts1}^*	fundamental current command in M-axis and T-axis
i_{Ms3}^* and i_{Ts3}^*	third harmonic current command in M-axis and T-axis
$\widehat{I_f}$ and $\widehat{I_t}$	RMS sequence value of fundamental and third harmonic currents under healthy condition
$\overline{I_{f1}}$-$\overline{I_{f5}}$	five-phase fundamental current phasor
$\overline{I_{t1}}$-$\overline{I_{t5}}$	five-phase third harmonic current phasor
$\overline{I_{nk}}$	stator sequence current with harmonic order n and sequence order k
$\overline{I_{nk}}^r$	rotor sequence current with harmonic order n and sequence order k
T_{eav}	average torque
ΔT_e^{14} and ΔT_e^{32}	ripple torque

The associate editor coordinating the review of this manuscript and approving it for publication was Zhixiang Zou.

P_{tl}	total copper loss
$\overline{V_{nk}}$	sequence voltage with harmonic order n and sequence order k
s_{nk}	motor slip with harmonic order n and sequence order k
p	pole pair number
ψ_m	phase margin
ϕ_{mnk}	air-gap flux with harmonic order n and sequence order k
V_{dc}	dc-link voltage
$E\hat{M}F_a - E\hat{M}F_e$	five-phase estimated electromotive force
k_p and τ_i	proportional resonant controller gains
T_d	transport delay
$\Im$	take an imaginary part
t	time
$*$	conjugate complex
MMF	magnetomotive force
IM	induction motor
SC	symmetrical component
EMF	electromotive force
PR	proportional resonant

I. INTRODUCTION

Multiphase motors have been widely used in air-craft drives, locomotive traction, electric ship propulsion and high-power industrial applications [1], [2]. As the number of phases increases, the required stator current amplitude can be reduced without changing phase voltages and output power [3], [4]. Besides, multiphase motors have competitive advantages over three-phase motors such as lower torque pulsations, higher power density, lower dc-link current harmonics and better power distribution among a higher number of phases [5], [6]. The fault-tolerant capability is one of the most interesting topics in multiphase stand-alone drives since no additional hardware is required if they are properly configured [7]. Various kinds of faults may occur in the motor drive system, while the power switching devices and the machine windings are the most vulnerable [8], [9]. According to [10], the possibility of faults on the switching devices is much higher than that on machine windings, and more than 70% of the faults would finally turn to open-circuit faults. Under the fault conditions, due to the redundant degrees of freedom, the multiphase motors can continue to operate with a lighter load even though no fault-tolerant control strategies are used [11]. One or more faulty phases lead to the asymmetry of power supply, which would affect the rotating trajectory of the air-gap MMF and finally result in serious torque ripple. Therefore, fault-tolerant control strategies are required to suppress the torque ripple and improve the output power. There are mainly two types of fault-tolerant control strategies for multiphase IMs in the existing literatures: Model-based and MMF based methods.

Several model-based methods have been presented in [2], [12]–[15]. When an open-phase fault appears, the conventional Park transformation matrix should be reconstructed

because of the asymmetry in the stator phase currents. Therefore, a reduced order model of a dual three-phase IM using decomposition transformation based on an asymmetrical winding structure is presented in [12], and the dynamics of the motor can be decomposed using an *M-T* plane model to represent the electromechanical energy [13]. Kianinezhad *et al*. compute the steady-state electromagnetic torque oscillations of a six-phase symmetrical IM. The magnitude of the pulsating torque depends on the difference between the $\alpha\beta$-subspace current components [14]. By using the same modeling approach, the pulsating torque components are eliminated for a five-phase and nine-phase motor, respectively [2], [15]. However, for the multiphase concentrated-full-pitch winding IM, the reconstruction of the Park transformation matrix cannot provide a diagonal mutual inductance matrix (L_{sr}) in the $\alpha\beta$ reference frame. Hence the torque cannot be decoupled, and the torque ripple still exists during post-fault operation under single-phase fault [2], [15]. The model-based methods can only be used in the motor with sinusoidal distributed winding structure, and the coupling between spatial harmonic fields limits its use in the concentrated-full-pitch winding IM.

The MMF-based methods do not depend on the motor model, and the current commands are required to ensure the invariance of the stator MMF [16], [17]. With this constraint, there are four different fault tolerant control strategies, e.g., the maximum torque strategy [18], [19], the minimum copper loss strategy [20], [21], the best flux distribution strategy [22], [23], and the minimum torque ripple strategy [16], [24], [25]. Specifically, the torque ripple needs to be minimized in the drive train and marine propulsion, because the high-magnitude torque ripple yields serious vibration and acoustic noise which, in turn, affect their lifetime [26], [27]. In the heathy case under fundamental power supply, only the fundamental MMF exists and it moves along the circular trajectory. In the open-phase faults case, the third harmonic MMFs appear which rotate at $\pm\omega/3$, and the interaction between the fundamental MMF and third harmonic MMFs leads to the torque ripple [16]. Therefore, the conventional minimum torque ripple strategy makes the fundamental current space vector to move along the circular trajectory in order to eliminate the coupling [25].

Regarding the harmonic current injection in the healthy case, the air-gap flux distribution is nearly rectangular and the fundamental air-gap flux can be larger than the rated value, thus the torque density and the iron utilization are improved [28]–[30]. However, during the post-fault operation, the third harmonic current space vector will generates the coupled fundamental MMF rotating at $\pm 3\omega$. Hence the coupling between the fundamental MMF and the spatial harmonic MMFs is more complex, and the torque ripple cannot be treated simply through the analysis of current space vectors. For example, when the maximum torque strategy is used for a five-phase IM with third harmonic current injection, there is no difference for the torque ripple between the post-fault condition and the fault condition [17].

The current space vector moves along the elliptical trajectory, which only illustrates the existence of the torque ripple. But the high-amplitude torque ripple cannot be explained because the relationship between the MMF and the torque ripple is ignored. Similarly, the torque ripple is suppressed indirectly from the conventional strategy based on the current space vector, and it is necessary to analyze and suppress the torque ripple in an analytical way.

SC theory was first proposed in 1918 to analyze the steady-state performance under asymmetrical power supply [31], and it has been used widely in the multiphase drive applications [20], [22], [32]–[36]. Because of the MMF coupling for the multiphase IM under open-phase faults, the torque cannot be decoupled using traditional multiphase Park transformation. However, based on SC transformation, positive and negative sequence currents in all harmonic subspaces can be decomposed. As a result, the steady-state equivalent circuit model of a five-phase IM is established, and the effect of stator winding connection on the performance can also be analyzed [32], [33]. Moreover, according to the constraints associated with the fault phase and optimization objective, the current commands under open-phase faults can be deduced [20], [22]. In addition, based on the features of SCs under fault conditions, a robust fault detection method was proposed for a five-phase motor in [34]. In order to suppress low frequency current harmonics and improve the stability of the current controller, the positive and negative sequence currents related to all SCs are controlled in the rotating frame separately [35], [36].

In this paper, based on the five-phase steady-state model using SCs, the torque ripple is mainly related to the first and fourth SCs because these two SCs interact with the fundamental mutual inductance (fundamental mutual inductance is nine times larger the third harmonic mutual inductance). Hence the first and fourth SCs need to be suppressed in order to minimize the torque ripple. Then based on the stator MMF invariance, several possible current commands are deduced under single-phase fault and two-phase fault. Moreover, third harmonic current injection is considered. By comparing their performance in terms of torque ripple, average torque and efficiency, the optimum strategy is selected and the effectiveness of the proposed strategy is validated by experimental results.

II. OPEN-PHASE FAULTS ANALYSIS USING STEADY-STATE MODEL IN TERMS OF SYMMETRICAL COMPONENTS

A. STEADY-STATE MODEL

The SC transformation for a five-phase system is given as

$$[A] = \frac{1}{5}\begin{bmatrix} 1 & a & a^2 & a^3 & a^4 \\ 1 & a^2 & a^4 & a^6 & a^8 \\ 1 & a^3 & a^6 & a^9 & a^{12} \\ 1 & a^4 & a^8 & a^{12} & a^{16} \\ 1 & 1 & 1 & 1 & 1 \end{bmatrix} \quad (1)$$
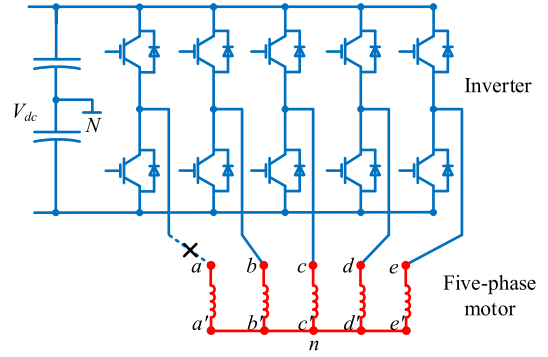

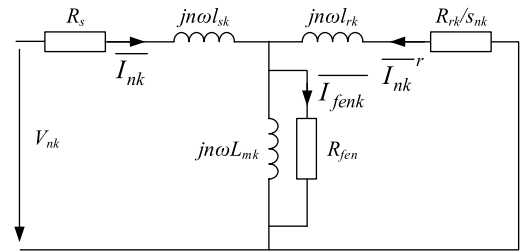FIGURE 1. Schematic diagram of the five-phase motor drive.

FIGURE 2. Five-phase induction motor equivalent circuit for any sequence *k*.

where a is $e^{j\frac{2\pi}{5}}$. A general scheme of the five-phase motor drive is shown in Fig. 1, the five-phase IM winding is connected in star with an isolated neutral point, and the steady state zero sequence current is equal to zero. The relationship between phase values and sequence values can be found by using the transformation $[A]$ and it is given as

$$\begin{bmatrix} \overline{I_{11}} \\ \overline{I_{12}} \\ \overline{I_{13}} \\ \overline{I_{14}} \\ 0 \end{bmatrix} + \begin{bmatrix} \overline{I_{31}} \\ \overline{I_{32}} \\ \overline{I_{33}} \\ \overline{I_{34}} \\ 0 \end{bmatrix} = [A]\left(\begin{bmatrix} \overline{I_{f1}} \\ \overline{I_{f2}} \\ \overline{I_{f3}} \\ \overline{I_{f4}} \\ \overline{I_{f5}} \end{bmatrix} + \begin{bmatrix} \overline{I_{t1}} \\ \overline{I_{t2}} \\ \overline{I_{t3}} \\ \overline{I_{t4}} \\ \overline{I_{t5}} \end{bmatrix} \right) \quad (2)$$

The steady-state model based on the SC theory under fundamental power supply is established in [32]. In order to analyze the torque ripple with third harmonic current injection, the work in [32] is extended into a more general model and the model contains eight sequence circuits. The equivalent circuit is shown in Fig. 2. The iron core loss consists of hysteresis loss and eddy loss. Because the slip frequency is generally much smaller than the stator frequency, the rotor iron core losses is neglected and only the stator iron core loss is considered [37].

$$P_{hynk} = 5k_{hy}\phi_{mnk}^2 |n\omega| \quad (3)$$

$$P_{ednk} = 5k_{ed}\phi_{mnk}^2 |n\omega|^2 \quad (4)$$

Then the iron loss can be represented in the equivalent circuit through an iron loss resistance R_{fen}, and is only valid when $\omega \neq 0$. The saturation will induce a third harmonic

TABLE 1. Motor slip distribution for any sequence *K*.

s_{1k}	Value	s_{3k}	Value
s_{11}	s	s_{31}	$(2+s)/3$
s_{12}	$4-3s$	s_{32}	$2-s$
s_{13}	$3s-2$	s_{33}	s
s_{14}	$2-s$	s_{34}	$(4-s)/3$

component in the stator currents. According to [33], the effect of this component can be ignored because the average torque of the five-phase motor is mainly produced by the fundamental currents.

$$R_{fen} = \frac{n\omega}{n\omega k_{ed} + k_{hy}} \tag{5}$$

where *n* is the harmonic order of 1 or 3. The rotor current $\overline{I_{nk}}^r$ is given as

$$\overline{I_{nk}}^r = \overline{I_{nk}} \frac{jn\omega L_{mk}R_{fen}/(jn\omega L_{mk} + R_{fen})}{jn\omega L_{mk}R_{fen}/(jn\omega L_{mk} + R_{fen}) + R_{rk}/s_{nk} + jn\omega l_{0rk}} \tag{6}$$

The iron core current $\overline{I_{nk}}^r$ is

$$\overline{I_{fenk}} = (\overline{I_{nk}} + \overline{I_{nk}}^r) \frac{jn\omega L_{mk}}{R_{fen} + jn\omega L_{mk}} \tag{7}$$

The motor slip s_{nk} related to sequence *k* and the harmonic order *n* is given as

$$s_{nk} = \frac{\omega_{nk} - \omega_r}{\omega_{nk}} \tag{8}$$

where ω_{nk} corresponding to the sequence *k* is given as

$$\omega_{nk} = \begin{cases} \dfrac{2\pi n f_s}{k} & (odd\ k) \\ \dfrac{2\pi n f_s}{(k-5)} & (even\ k) \end{cases} \tag{9}$$

According to (8) and (9), the value of s_{nk} distribution is shown in Table 1 and s_{11} is defined as *s*.

The torque of the five-phase motor under unbalanced operation is produced by all the SCs, and the results of the average torque and ripple torque are:

$$T_e(t) = T_{eav} + \Delta T_e^{14} + \Delta T_e^{32} \tag{10}$$

$$T_{eav} = 5pL_{m1}\Im(\overline{I_{11}I_{11}}^{r*} + \overline{I_{14}}^*\overline{I_{14}}^r + \overline{I_{31}I_{31}}^{r*} + \overline{I_{34}}^*\overline{I_{34}}^r)$$
$$+ 15pL_{m3}\Im(\overline{I_{13}I_{13}}^{r*} + \overline{I_{12}}^*\overline{I_{12}}^r + \overline{I_{33}I_{33}}^{r*} + \overline{I_{32}}^*\overline{I_{32}}^r) \tag{11}$$

$$\Delta T_e^{14} = 5pL_{m1}\Im\{(\overline{I_{11}I_{14}}^r + \overline{I_{14}}^*\overline{I_{34}}^r + \overline{I_{31}I_{11}}^{r*})e^{j2\omega t}$$
$$+ (\overline{I_{11}I_{31}}^{r*} + \overline{I_{14}}^*\overline{I_{11}}^{r*} + \overline{I_{34}}^*\overline{I_{14}}^r)e^{-j2\omega t}$$
$$+ (\overline{I_{11}I_{34}}^r + \overline{I_{31}I_{14}}^r)e^{j4\omega t}$$
$$+ (\overline{I_{14}}^*\overline{I_{31}}^{r*} + \overline{I_{34}}^*\overline{I_{11}}^{r*})e^{-j4\omega t}$$
$$+ \overline{I_{31}I_{34}}^r e^{j6\omega t} + \overline{I_{34}}^*\overline{I_{31}}^{r*}e^{-j6\omega t}\} \tag{12}$$

$$\Delta T_e^{32} = 15pL_{m3}\Im\{(\overline{I_{13}I_{12}}^r + \overline{I_{12}}^*\overline{I_{32}}^r + \overline{I_{33}I_{13}}^{r*})e^{j2\omega t}$$
$$+ (\overline{I_{12}}^*\overline{I_{13}}^{r*} + \overline{I_{32}}^*\overline{I_{12}}^r + \overline{I_{13}I_{33}}^{r*})e^{-j2\omega t}$$
$$+ (\overline{I_{13}I_{32}}^r + \overline{I_{33}I_{12}}^r)e^{j4\omega t}$$
$$+ (\overline{I_{12}}^*\overline{I_{33}}^{r*} + \overline{I_{32}}^*\overline{I_{13}}^{r*})e^{-j4\omega t}$$
$$+ \overline{I_{33}I_{32}}^r e^{j6\omega t} + \overline{I_{32}}^*\overline{I_{33}}^{r*}e^{-j6\omega t}\} \tag{13}$$

The total copper loss including the stator copper loss, rotor copper loss and iron core loss is given as

$$P_{tl} = 5(|\overline{I_{11}}|^2 + |\overline{I_{12}}|^2 + |\overline{I_{13}}|^2 + |\overline{I_{14}}|^2$$
$$+ |\overline{I_{31}}|^2 + |\overline{I_{32}}|^2 + |\overline{I_{33}}|^2 + |\overline{I_{34}}|^2)R_s$$
$$+ 5(|\overline{I_{11}}^r|^2 + |\overline{I_{14}}^r|^2 + |\overline{I_{31}}^r|^2 + |\overline{I_{34}}^r|^2)R_{r1}$$
$$+ 5(|\overline{I_{12}}^r|^2 + |\overline{I_{13}}^r|^2 + |\overline{I_{32}}^r|^2 + |\overline{I_{33}}^r|^2)R_{r3}$$
$$+ 5(|\overline{I_{fe11}}|^2 + |\overline{I_{fe12}}|^2 + |\overline{I_{fe13}}|^2 + |\overline{I_{fe14}}|^2)R_{fe1}$$
$$+ 5(|\overline{I_{fe31}}|^2 + |\overline{I_{fe32}}|^2 + |\overline{I_{33}}|^2 + |\overline{I_{34}}|^2)R_{fe3} \tag{14}$$

At the same time, the efficiency is a key factor and its expression is

$$Efficiency = \frac{T_{eav}\omega/p}{T_{eav}\omega/p + P_{tl}} \tag{15}$$

B. TORQUE RIPPLE ANALYSIS

The SC distribution of five-phase fundamental and third harmonic currents under healthy condition is

$$\begin{cases} \overline{I_{11}} = \widehat{I_f} \angle 0 \\ \overline{I_{33}} = \widehat{I_t} \angle 0 \\ \overline{I_{12}} = \overline{I_{13}} = \overline{I_{14}} = \overline{I_{31}} = \overline{I_{32}} = \overline{I_{34}} = 0 \end{cases} \tag{16}$$

The fundamental MMF is only produced by $\overline{I_{11}}$ and the third harmonic MMF is only produced by $\overline{I_{33}}$, hence no torque ripple exists. When phase "a" is under open circuit, $\overline{I_{f1}}$ and $\overline{I_{t1}}$ are zero. According to (2), the constraint associated with phase "a" is

$$\begin{cases} \overline{I_{11}} + \overline{I_{12}} + \overline{I_{13}} + \overline{I_{14}} = 0 \\ \overline{I_{31}} + \overline{I_{32}} + \overline{I_{33}} + \overline{I_{34}} = 0 \end{cases} \tag{17}$$

Similarly, when phase "a" and phase "b" are under open circuit, the constraint is

$$\begin{cases} \overline{I_{11}} + \overline{I_{12}} + \overline{I_{13}} + \overline{I_{14}} = 0 \\ a^{-1}\overline{I_{11}} + a^{-2}\overline{I_{12}} + a^{-3}\overline{I_{13}} + a^{-4}\overline{I_{14}} = 0 \\ \overline{I_{31}} + \overline{I_{32}} + \overline{I_{33}} + \overline{I_{34}} = 0 \\ a^{-1}\overline{I_{31}} + a^{-2}\overline{I_{32}} + a^{-3}\overline{I_{33}} + a^{-4}\overline{I_{34}} = 0 \end{cases} \tag{18}$$

For the non-adjacent two-phase fault (phase "a" and phase "c" are under open circuit), the constraint is

$$\begin{cases} \overline{I_{11}} + \overline{I_{12}} + \overline{I_{13}} + \overline{I_{14}} = 0 \\ a^{-2}\overline{I_{11}} + a^{-4}\overline{I_{12}} + a^{-6}\overline{I_{13}} + a^{-8}\overline{I_{14}} = 0 \\ \overline{I_{31}} + \overline{I_{32}} + \overline{I_{33}} + \overline{I_{34}} = 0 \\ a^{-2}\overline{I_{31}} + a^{-4}\overline{I_{32}} + a^{-6}\overline{I_{33}} + a^{-8}\overline{I_{34}} = 0 \end{cases} \tag{19}$$

Regarding the third harmonic current injection, all SCs $\overline{I_{11}}$-$\overline{I_{34}}$ are nonzero. According to (11)-(13), besides an average torque T_{eav}, there are also two pulsating components at three frequencies ($2f_s$, $4f_s$ and $6f_s$), i.e., ΔT_e^{14} and ΔT_e^{32}. Under the fundamental power supply, $\overline{I_{31}}$-$\overline{I_{34}}$ are zero and the torque pulsates at $2f_s$. In addition, ΔT_e^{14} is the product of L_{m1} and the function of first SC and fourth SC ($\overline{I_{11}}$, $\overline{I_{14}}$, $\overline{I_{31}}$ and $\overline{I_{34}}$), and ΔT_e^{32} is the product of L_{m3} and the function of second SC and third SC ($\overline{I_{12}}$, $\overline{I_{13}}$, $\overline{I_{32}}$ and $\overline{I_{33}}$). As L_{m1} is nine times larger than L_{m3}, the coefficient of ΔT_e^{14} is three times larger than that of ΔT_e^{32} and ΔT_e^{14} plays a key role in the torque ripple [32].

C. PERFORMANCE EVALUATION

Through the equivalent circuit model in Fig. 2, the torque ripple, average torque and efficiency can be calculated. In this paper, rotor field-oriented control is used to control the five-phase IM. The current commands in M-T axis are calculated to satisfy the demanded flux and torque [28].

$$\begin{cases} i_{Ms1}^* = \dfrac{\phi_r^*}{L_{m1}} \\[2mm] i_{Ms3}^* = \dfrac{1}{18}\dfrac{L_{m1}}{L_{m3}}i_{Ms1}^* \\[2mm] i_{Ts1}^* = \dfrac{T_e^*(L_{m1}+L_{0r1})}{p\phi_r^*L_{m1}(1+\frac{1}{36}\frac{R_{r1}}{R_{r3}})} \\[2mm] i_{Ts3}^* = \dfrac{1}{6}\dfrac{L_{m1}}{L_{m3}}\dfrac{L_{r3}}{L_{r1}}\dfrac{R_{r1}}{R_{r3}}i_{Ts1}^* \end{cases} \quad (20)$$

The first fundamental and third harmonic sequence currents $\overline{I_{11}}$ and $\overline{I_{33}}$ are

$$\begin{cases} \overline{I_{11}} = I_{m1}\angle(\arctan\dfrac{i_{Ts1}^*}{i_{Ms1}^*}-\dfrac{\pi}{2}) \\[3mm] \overline{I_{33}} = I_{m3}\angle(\arctan\dfrac{i_{Ts3}^*}{i_{Ms3}^*}-\dfrac{\pi}{2}) \end{cases} \quad (21)$$

The fundamental slip angle speed is given in (21).

$$\omega_{s1} = \dfrac{i_{Ts1}^* R_{r1}}{i_{Ms1}^*(L_{m1}+L_{0r1})} \quad (22)$$

The fundamental supply angle speed ω can be calculated through the sum of the slip angle speed ω_{s1} and a given speed ω_r. Then all the sequence currents in the equivalent circuit can be acquired using MATLAB script. The torque ripple, average torque and efficiency can be evaluated with the change of the speed and load, and the overall diagram is shown in Fig. 3.

III. TORQUE RIPPLE MINIMIZATION
A. CONVENTIONAL MINIMUM TORQUE RIPPLE STRATEGY UNDER SINGLE-PHASE FAULT

Based on the stator MMF invariance, the conventional strategy minimizes the torque ripple by suppressing the coupling between the fundamental MMF and the third harmonic MMF [25]. As shown in Fig. 4, the fundamental spatial plane is coupled with third harmonic spatial plane under
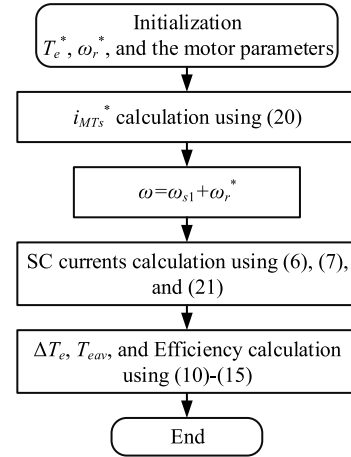
FIGURE 3. The diagram of the performance evaluation.

FIGURE 4. The relationship between the currents and MMF under open-phase faults. (a) Healthy condition, (b) Open-phase faults condition.

open-phase faults. The fundamental current space vector $\overrightarrow{i}_{s1}^1$ and $\overrightarrow{i}_{s1}^3$ produces two magnetic fields rotating at $\pm\omega$ and $\pm\omega/3$, respectively. Similarly, the third harmonic current space vector $\overrightarrow{i}_{s3}^1$ and $\overrightarrow{i}_{s3}^3$ also generates two magnetic fields rotating at $\pm3\omega$ and $\pm\omega$. In order to suppress the coupling, the reverse rotating current space vectors are removed. $\overrightarrow{i}_{s1}^3$ and $\overrightarrow{i}_{s3}^1$ are designed to force the coupled MMF to move along the forward circular trajectory, as shown in the Fig. 5(a) and Fig. 6(a). It is worth noting that all the MMFs are decoupled by sequence currents compared with the current space vector. $\overline{I_{11}}$, $\overline{I_{14}}$, $\overline{I_{31}}$ and $\overline{I_{34}}$ represent the fundamental MMFs and $\overline{I_{12}}$, $\overline{I_{13}}$, $\overline{I_{32}}$ and $\overline{I_{33}}$ represent the third harmonic MMFs, and their rotating speed is shown in Table 2.

However, the torque ripple is suppressed indirectly from the conventional strategy, and the analytical relationship between the MMF and the torque ripple is ignored. Therefore, it is necessary to reevaluate and suppress the torque ripple from its analytical expression. Through the

FIGURE 5. The MMF analysis under single-phase fault. (a) Conventional strategy (*CS*1), (b) Proposed strategy (*PS*1).
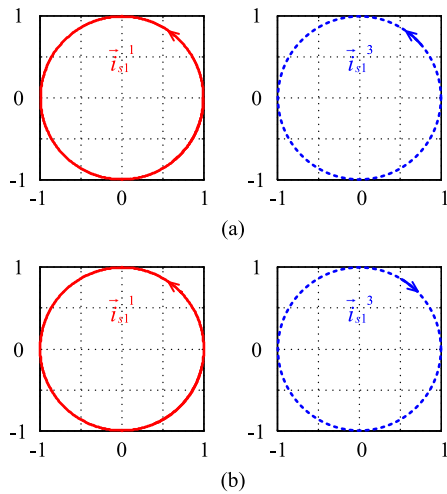

FIGURE 6. The trajectories of fundamental current space vector under single-phase fault. (a) Conventional strategy (*CS*1), (b) Proposed strategy (*PS*1).

TABLE 2. Rotating speed distribution for sequence currents.

$\overline{I_{1k}}$	Rotating speed	$\overline{I_{3k}}$	Rotating speed
$\overline{I_{11}}$	ω	$\overline{I_{31}}$	3ω
$\overline{I_{12}}$	$-\omega/3$	$\overline{I_{32}}$	$-\omega$
$\overline{I_{13}}$	$\omega/3$	$\overline{I_{33}}$	ω
$\overline{I_{14}}$	$-\omega$	$\overline{I_{34}}$	-3ω

TABLE 3. Rated parameters of the five-phase IM.

Parameter	Value	Parameter	Value
Rated power	5 kW	R_{r1}	8.1 mΩ
RMS current	72 A	R_{r3}	7.8 mΩ
Rated speed	1940 r/min	L_{m1}	1.58 mH
Rated torque	25 N·m	L_{m3}	0.18 mH
p	2	$L_{os1} = L_{os3}$	0.05 mH
R_s	11 mΩ	$L_{or1} = L_{or3}$	0.05 mH
f_{sw}	10 kHz	V_{dc}	72 V

(24) states that the ripple torque is zero under the fundamental power supply because $\overline{I_{31}}$-$\overline{I_{34}}$ are zero. However, if considering third harmonic current injection, the ripple torque will be large. Because ΔT_e^{14} appears and it plays a major role in the torque ripple according to S^S II. Moreover, the performance such as the torque ripple, average torque and efficiency are not evaluated in the conventional method.

B. PROPOSED MINIMUM TORQUE RIPPLE STRATEGY UNDER SIGLE-PHASE FAULT

Because ΔT_e^{14} plays a major role in the torque ripple, the first and fourth sequence currents are proposed to be suppressed in this paper. Under fundamental power supply, $\overline{I_{11}}$ is kept constant based on the stator MMF invariance. Combining the constraint in (17), two zero torque ripple solutions can be deduced. The first solution is same with the conventional minimum torque ripple strategy in (23). In the second solution (*PS*1), $\overline{I_{11}}$ and $\overline{I_{12}}$ are reserved as shown in (25).

$$PS1 \begin{cases} \overline{I_{11}} = \widehat{I_f} \angle 0 \\ \overline{I_{12}} = -\overline{I_{11}} \\ \overline{I_{14}} = \overline{I_{13}} = 0 \end{cases} \tag{25}$$

In order to compare the performance of *CS*1 and *PS*1, the current commands are introduced in the simulation model of S^S II. The rated parameters of five-phase IM is shown in Table 3. The comparison results as a function of the rotor speed under a 10 N·m load are presented in Fig. 7. The comparison in terms of peak-to-peak amplitude of torque ripple (in p.u of the load torque) is presented in Fig. 7(a).
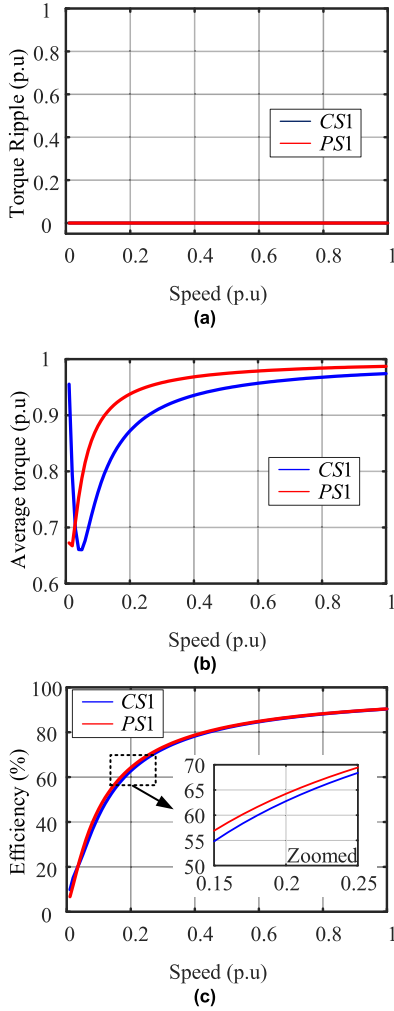
SC transformation, the SC distribution of the conventional strategy under phase "*a*" open (*CS*1) is

$$CS1 \begin{cases} \overline{I_{11}} = \widehat{I_f} \angle 0 \\ \overline{I_{13}} = -\overline{I_{11}} \\ \overline{I_{12}} = \overline{I_{14}} = 0 \\ \overline{I_{33}} = \widehat{I_t} \angle 0 \\ \overline{I_{31}} = -\overline{I_{33}} \\ \overline{I_{32}} = \overline{I_{34}} = 0 \end{cases} \tag{23}$$

where $\overline{I_{11}}$ and $\overline{I_{33}}$ are same with the healthy condition in order to keep the stator MMF invariance. Introducing (23) into (12) and (13), the ripple torque is

$$\begin{cases} \Delta T_{eCS1}^{14} = 5pL_{m1}\Im\{\overline{I_{31}I_{11}}^{r*}e^{j2\omega t} + \overline{I_{11}I_{31}}^{r*}e^{-j2\omega t}\} \\ \Delta T_{eCS1}^{32} = 15pL_{m3}\Im\{\overline{I_{33}I_{13}}^{r*}e^{j2\omega t} + \overline{I_{13}I_{33}}^{r*}e^{-j2\omega t}\} \end{cases} \tag{24}$$

FIGURE 7. Characteristic curves for *CS*1 strategy and *PS*1 strategy under fundamental power supply. (a) Torque ripple, (b) Average torque, (c) Efficiency.

As expected, *CS*1 and *PS*1 generate no torque ripple in the whole speed range. *PS*1 achieves larger average torque than *CS*1 except in the low speed range, as shown in Fig. 7(b). According to Fig. 7(c), *PS*1 achieves higher efficiency than *CS*1. As shown in Fig. 6, the rotating direction of trajectories of current space vector $\overrightarrow{i}_{s1}^{3}$ is opposite between *CS*1 and *PS*1. To sum up, it is better to choose *PS*1 under fundamental supply to suppress the torque ripple as it not only achieves no torque ripple, but also a higher average torque and higher efficiency compared with *CS*1.

In terms of the third harmonic current injection, $\overline{I}_{33}$ and $\overline{I}_{32}$ are reserved in *PS*1. The SC distribution of third harmonic sequence currents of the proposed strategy is

$$PS1 \begin{cases} \overline{I}_{33} = \widehat{I}_t \angle 0 \\ \overline{I}_{32} = -\overline{I}_{33} \\ \overline{I}_{31} = \overline{I}_{34} = 0 \end{cases} \qquad (26)$$
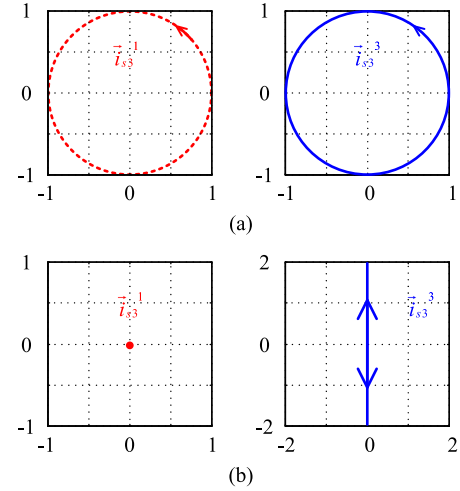

FIGURE 8. The trajectories of third harmonic current space vector under single-phase fault. (a) Conventional strategy (*CS*1), (b) Proposed strategy (*PS*1).

Combining with the fundamental sequence currents in (25), the ripple torque is

$$\Delta T_{ePS1}^{32} = 15pL_{m3}\Im\{\overline{I}_{12}^{*}\overline{I}_{32}^{r}e^{j2\omega t} + \overline{I}_{32}^{*}\overline{I}_{12}^{r}e^{-j2\omega t} \\ + \overline{I}_{33}\overline{I}_{12}^{r}e^{j4\omega t} + \overline{I}_{12}^{*}\overline{I}_{33}^{r*}e^{-j4\omega t} \\ + \overline{I}_{33}\overline{I}_{32}^{r}e^{j6\omega t} + \overline{I}_{32}^{*}\overline{I}_{33}^{r*}e^{-j6\omega t}\} \qquad (27)$$

From (24) and (27), ΔT_e^{14} of the proposed strategy is zero and only ΔT_e^{32} exists. Besides, the ripple torque of the conventional strategy includes ΔT_e^{32} and ΔT_e^{14} at the same time. Hence the proposed strategy suppresses the torque ripple further compared with the conventional strategy. According to Fig. 8, although the trajectories of $\overrightarrow{i}_{s3}^{1}$ and $\overrightarrow{i}_{s3}^{3}$ rotate in the same direction, the interaction between $\overrightarrow{i}_{s3}^{1}$ and $\overrightarrow{i}_{s1}^{1}$ is ignored. The proposed strategy eliminates the $\overrightarrow{i}_{s3}^{1}$ and the trajectory of $\overrightarrow{i}_{s3}^{3}$ moves up and down in one period. Hence the torque ripple will be smaller, and the MMF analysis is shown in Fig. 5(b). Similarly, introducing (23), (25) and (26) into the simulation model of S^S II, the results of comparison under a 10 N·m load is shown in Fig. 9 and the reference torque is equal to the load torque. As shown in Fig. 9(a), *CS*1 produces larger torque ripple than *PS*1 as a result of the existence of ΔT_e^{14}. According to Fig. 9(b), *PS*1 achieves a larger average torque than *CS*1 in most of the speed range. As it can be seen from Fig. 9(c), *PS*1 achieves also a higher efficiency than *CS*1 in most of the speed ranges. To sum up, *PS*1 shows better performance than *CS*1 in terms of the torque ripple, average torque and efficiency.

C. CONVENTIONAL MINIMUM TORQUE RIPPLE STRATEGY UNDER TWO-PHASE FAULT

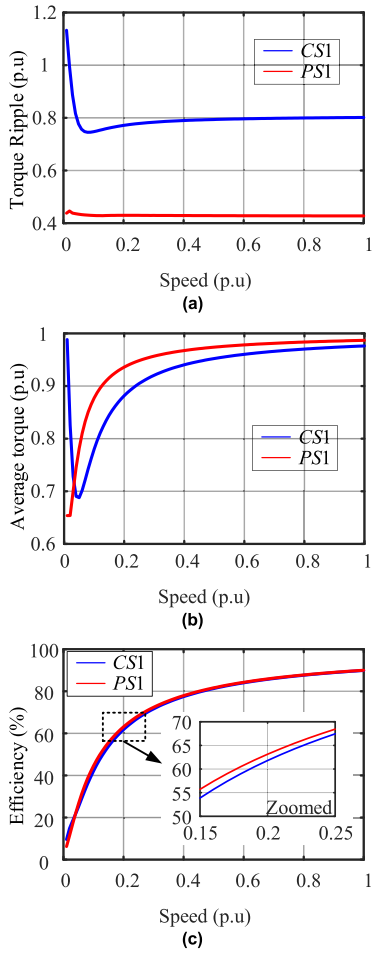Under two-phase fault, there are only three phase remaining and the control freedom is reduced. Hence there is

FIGURE 9. Characteristic curves for *CS*1 strategy and *PS*1 strategy with third harmonic injection. (a) Torque ripple, (b) Average torque, (c) Efficiency.

FIGURE 10. The MMF analysis under two-phase faults. (a) Conventional strategy (*CS*2), (b) Proposed strategy (*PS*2-1), (c) Proposed strategy (*PS*2-2).

a unique solution for the fundamental currents based on the MMF invariance. In order to suppress the torque ripple under third harmonic current injection, $\overrightarrow{i}\,^1_{s3}$ is designed to force the coupled MMF moving along the forward circular trajectory, as shown in Fig. 10(a). The SC distribution of the conventional strategy (*CS*2) under phase "*a*" and phase "*b*" open is

$$CS2_{ab} \begin{cases} \overline{I_{11}} = \widehat{I_f} \angle 0 \\ \overline{I_{12}} = 1.618\overline{I_{11}} \angle -\dfrac{4\pi}{5} \\ \overline{I_{13}} = \overline{I_{11}} \angle \dfrac{2\pi}{5} \\ \overline{I_{14}} = 0 \\ \overline{I_{33}} = \overline{I_{31}} \angle \dfrac{2\pi}{5} \\ \overline{I_{31}} = \widehat{I_t} \angle 0 \\ \overline{I_{32}} = 1.618\overline{I_{31}} \angle -\dfrac{4\pi}{5} \\ \overline{I_{34}} = 0 \end{cases} \quad (28)$$

Similarly, the SC distribution of the conventional strategy (*CS*2) under phase "*a*" and phase "*c*" open is

$$CS2_{ac} \begin{cases} \overline{I_{11}} = \widehat{I_f} \angle 0 \\ \overline{I_{12}} = 0.618\overline{I_{11}} \angle -\dfrac{3\pi}{5} \\ \overline{I_{13}} = \overline{I_{11}} \angle \dfrac{4\pi}{5} \\ \overline{I_{14}} = 0 \\ \overline{I_{33}} = \overline{I_{31}} \angle \dfrac{4\pi}{5} \\ \overline{I_{31}} = \widehat{I_t} \angle 0 \\ \overline{I_{32}} = 0.618\overline{I_{31}} \angle -\dfrac{3\pi}{5} \\ \overline{I_{34}} = 0 \end{cases} \quad (29)$$

The trajectories of third harmonic current space vector under adjacent and non-adjacent two phase fault are shown in Fig. 11(a) and Fig. 12(a). Introducing (28) and (29) into (12) and (13), the ripple torque expressions for adjacent fault and non-adjacent fault are same, which are given as

$$\Delta T^{14}_{eCS2} = 5pL_{m1}\Im\{(\overline{I_{31}I_{11}}^{r*})e^{j2\omega t} + (\overline{I_{11}I_{31}}^{r*})e^{-j2\omega t}\}$$
$$\Delta T^{32}_{eCS2} = 15pL_{m3}\Im\{(\overline{I_{13}I_{12}}^{r} + \overline{I_{12}}^{*}\overline{I_{32}}^{r} + \overline{I_{33}I_{13}}^{r*})e^{j2\omega t}$$
$$+ (\overline{I_{12}}^{*}\overline{I_{13}}^{r*} + \overline{I_{32}}^{*}\overline{I_{12}}^{r} + \overline{I_{13}I_{33}}^{r*})e^{-j2\omega t}$$
$$+ (\overline{I_{13}I_{32}}^{r} + \overline{I_{33}I_{12}}^{r})e^{j4\omega t}$$
$$+ (\overline{I_{12}}^{*}\overline{I_{33}}^{r*} + \overline{I_{32}}^{*}\overline{I_{13}}^{r*})e^{-j4\omega t}$$
$$+ \overline{I_{33}I_{32}}^{r}e^{j6\omega t} + \overline{I_{32}}^{*}\overline{I_{33}}^{r*}e^{-j6\omega t}\} \quad (30)$$

FIGURE 11. The trajectories of third harmonic current space vector under adjacent two phase fault. (a) Conventional strategy (CS2$_{ab}$), (b) Proposed strategy (PS2-1$_{ab}$), (c) Proposed strategy (PS2-2$_{ab}$).
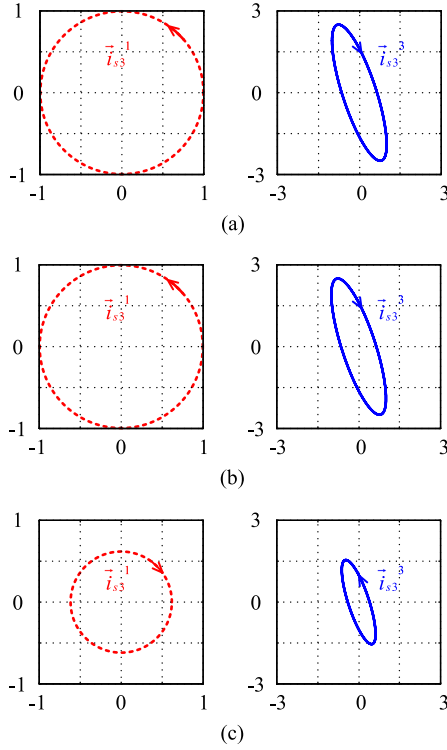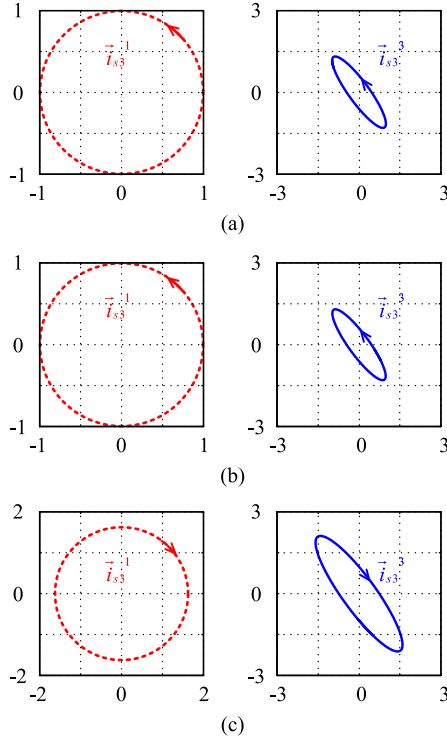

FIGURE 12. The trajectories of third harmonic current space vector under non-adjacent two phase fault. (a) Conventional strategy (CS2$_{ac}$), (b) Proposed strategy (PS2-1$_{ac}$), (c) Proposed strategy (PS2-2$_{ac}$).

(30) states that the conventional strategy generates ΔT_{e14} and ΔT_{e32} at the same time under two-phase fault. However, according to the constraint in (18) and (19), there are also

other solutions to suppress the torque ripple and the conventional strategy may not be the optimum solution under third harmonic current injection.

D. PROPOSED MINIMUM TORQUE RIPPLE STRATEGY UNDER TWO-PHASE FAULT

Similarly, the fundamental sequence currents are same with the conventional strategy based on the constraint in (18)-(19) and the fundamental MMF invariance. In terms of third harmonic currents optimization, the $\overline{I_{33}}$ is still kept constant in order to maintain the same third harmonic MMF. Based on the constraint in (18)-(19), there are two solutions by eliminating $\overline{I_{34}}$ (PS2-1) or $\overline{I_{31}}$ (PS2-2). The SC distribution for the adjacent and non-adjacent two-phase fault are given in (31)-(34).

$$PS2-1_{ab}\begin{cases} \overline{I_{11}} = \widehat{I_f}\angle 0 \\ \overline{I_{12}} = 1.618\overline{I_{11}}\angle -\dfrac{4\pi}{5} \\ \overline{I_{13}} = \overline{I_{11}}\angle\dfrac{2\pi}{5} \\ \overline{I_{14}} = 0 \\ \overline{I_{33}} = \widehat{I_t}\angle 0 \\ \overline{I_{31}} = \overline{I_{33}}\angle -\dfrac{2\pi}{5} \\ \overline{I_{32}} = 1.618\overline{I_{33}}\angle\dfrac{4\pi}{5} \\ \overline{I_{34}} = 0 \end{cases} \quad (31)$$

$$PS2-2_{ab}\begin{cases} \overline{I_{11}} = \widehat{I_f}\angle 0 \\ \overline{I_{12}} = 1.618\overline{I_{11}}\angle -\dfrac{4\pi}{5} \\ \overline{I_{13}} = \overline{I_{11}}\angle\dfrac{2\pi}{5} \\ \overline{I_{14}} = 0 \\ \overline{I_{33}} = \widehat{I_t}\angle 0 \\ \overline{I_{31}} = 0 \\ \overline{I_{32}} = 0.618\overline{I_{33}}\angle\dfrac{4\pi}{5} \\ \overline{I_{34}} = 0.618\overline{I_{33}}\angle -\dfrac{4\pi}{5} \end{cases} \quad (32)$$

$$PS2-1_{ac}\begin{cases} \overline{I_{11}} = \widehat{I_f}\angle 0 \\ \overline{I_{12}} = 1.618\overline{I_{11}}\angle -\dfrac{4\pi}{5} \\ \overline{I_{13}} = \overline{I_{11}}\angle\dfrac{2\pi}{5} \\ \overline{I_{14}} = 0 \\ \overline{I_{33}} = \widehat{I_t}\angle 0 \\ \overline{I_{31}} = \overline{I_{33}}\angle -\dfrac{2\pi}{5} \\ \overline{I_{32}} = 1.618\overline{I_{33}}\angle\dfrac{4\pi}{5} \\ \overline{I_{34}} = 0 \end{cases} \quad (33)$$

$$PS2 - 2_{ac} \begin{cases} \overline{I_{11}} = \widehat{I_f} \angle 0° \\ \overline{I_{12}} = 1.618\overline{I_{11}} \angle -\dfrac{4\pi}{5} \\ \overline{I_{13}} = \overline{I_{11}} \angle \dfrac{2\pi}{5} \\ \overline{I_{14}} = 0 \\ \overline{I_{33}} = \widehat{I_t} \angle 0° \\ \overline{I_{31}} = 0 \\ \overline{I_{32}} = 0.618\overline{I_{33}} \angle \dfrac{4\pi}{5} \\ \overline{I_{34}} = 0.618\overline{I_{33}} \angle -\dfrac{4\pi}{5} \end{cases} \quad (34)$$

Introducing (31)-(34) into (12) and (13), the ripple torque of *PS*2-1 and *PS*2-2 are

$$\Delta T_{ePS2-1}^{14} = 5pL_{m1}\Im\{(\overline{I_{31}I_{11}}^{r*})e^{j2\omega t} + (\overline{I_{11}I_{31}}^{r*})e^{-j2\omega t}\}$$

$$\Delta T_{ePS2-1}^{32} = 15pL_{m3}\Im\{(\overline{I_{13}I_{12}}^{r} + \overline{I_{12}}^*\overline{I_{32}}^{r} + \overline{I_{33}I_{13}}^{r*})e^{j2\omega t}$$
$$\qquad + (\overline{I_{12}}^*\overline{I_{13}}^{r*} + \overline{I_{32}}^*\overline{I_{12}}^{r} + \overline{I_{13}I_{33}}^{r*})e^{-j2\omega t}$$
$$\qquad + (\overline{I_{13}I_{32}}^{r} + \overline{I_{33}I_{12}}^{r})e^{j4\omega t}$$
$$\qquad + (\overline{I_{12}}^*\overline{I_{33}}^{r*} + \overline{I_{32}}^*\overline{I_{13}}^{r*})e^{-j4\omega t}$$
$$\qquad + \overline{I_{33}I_{32}}^{r}e^{j6\omega t} + \overline{I_{32}}^*\overline{I_{33}}^{r*}e^{-j6\omega t}\} \quad (35)$$

$$\Delta T_{ePS2-2}^{14} = 5pL_{m1}\Im\{\overline{I_{11}I_{34}}^{r}e^{j4\omega t} + \overline{I_{34}}^*\overline{I_{11}}^{r*}e^{-j4\omega t}\}$$

$$\Delta T_{ePS2-2}^{32} = 15pL_{m3}\Im\{(\overline{I_{13}I_{12}}^{r} + \overline{I_{12}}^*\overline{I_{32}}^{r} + \overline{I_{33}I_{13}}^{r*})e^{j2\omega t}$$
$$\qquad + (\overline{I_{12}}^*\overline{I_{13}}^{r*} + \overline{I_{32}}^*\overline{I_{12}}^{r} + \overline{I_{13}I_{33}}^{r*})e^{-j2\omega t}$$
$$\qquad + (\overline{I_{13}I_{32}}^{r} + \overline{I_{33}I_{12}}^{r})e^{j4\omega t}$$
$$\qquad + (\overline{I_{12}}^*\overline{I_{33}}^{r*} + \overline{I_{32}}^*\overline{I_{13}}^{r*})e^{-j4\omega t}$$
$$\qquad + \overline{I_{33}I_{32}}^{r}e^{j6\omega t} + \overline{I_{32}}^*\overline{I_{33}}^{r*}e^{-j6\omega t}\} \quad (36)$$

According to (30), (35) and (36), the ripple torque of *CS*2 is same with *PS*2-1. The difference between *PS*2-1 and *PS*2-2 lies in ΔT_e^{14}. Besides, the MMF distribution of *PS*2-1 is same with *CS*2, as shown in Fig. 10(b), Fig. 11(b) and Fig. 12(b). The forward coupled fundamental MMF is removed in *PS*2-2, and the trajectory of $\overrightarrow{i}_3^1$ rotates at -3ω, as shown in Fig. 10(c), Fig. 11(c) and Fig. 12(c). In order to choose the optimum strategy under two-phase fault, introducing (29) and (31)-(34) into the simulation model of S^S II, the results of comparison under a 5 N·m load is shown in Fig. 13-14 and the reference torque is equal to the load torque. Under adjacent two-phase fault, as shown in Fig. 13(a), *PS*2-1$_{ab}$ achieves the lowest torque ripple. But *CS*2$_{ab}$ achieves the highest average torque and efficiency, as shown in Fig. 13(b) and Fig. 13(c). It is worth noting that these three strategies shows a negative efficiency and average torque in the low speed range. Because the torque ripple is high, and the motor can continue to operate even though the average torque is negative. On the other hand, according to Fig. 14, *CS*2$_{ac}$ achieves lowest torque ripple among three strategies. Moreover, *CS*2$_{ac}$ shows a higher efficiency than other two strategies in most of the speed range. Because ΔT_e^{14} always exists for the two-phase fault, which strategy is better can only be determined through the performance analysis. To sum up, under adjacent
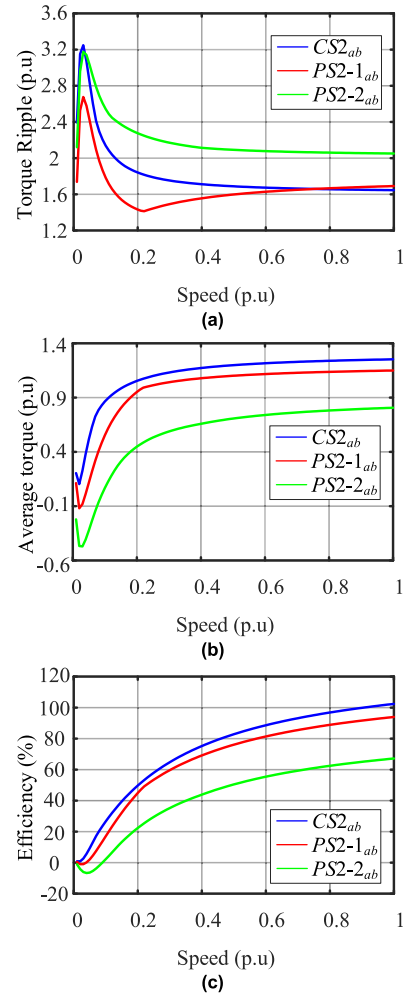

FIGURE 13. Characteristic curves for *CS*2$_{ab}$ strategy, *PS*2-1$_{ab}$ strategy and *PS*2-2$_{ab}$ strategy with third harmonic injection. (a) Torque ripple, (b) Average torque, (c) Efficiency.

two-phase fault, *PS*2-1$_{ab}$ achieves the lowest torque ripple but with a lower efficiency than *CS*2$_{ab}$. hence *CS*2$_{ab}$ and *PS*2-1$_{ab}$ can be selected according to the application requirements. Under non-adjacent two-phase fault, it is better to use *CS*2$_{ac}$ and there is no performance improvement for other two stratigies.

IV. FAULT-TOLERANT CURRENT CONTROL

The overall control diagram is shown in Fig. 15. The control system includes a current loop and a speed loop. i_{Ms1}^* is constant, and i_{Ts1}^* is determined by the PI regulator and the speed error. Through the inverse SC transformation, the current commands for the conventional strategy and the proposed strategy in the phase frame are deduced. Then a resilient current control scheme [18] is used to establish the relationship between the currents in the synchronous *MT* frame and phase frame, as shown in the appendix.

Because the phase currents are asymmetrical, a PR regulator is used in order to achieve a good response during post-fault operation and the resonant term has a large gain at
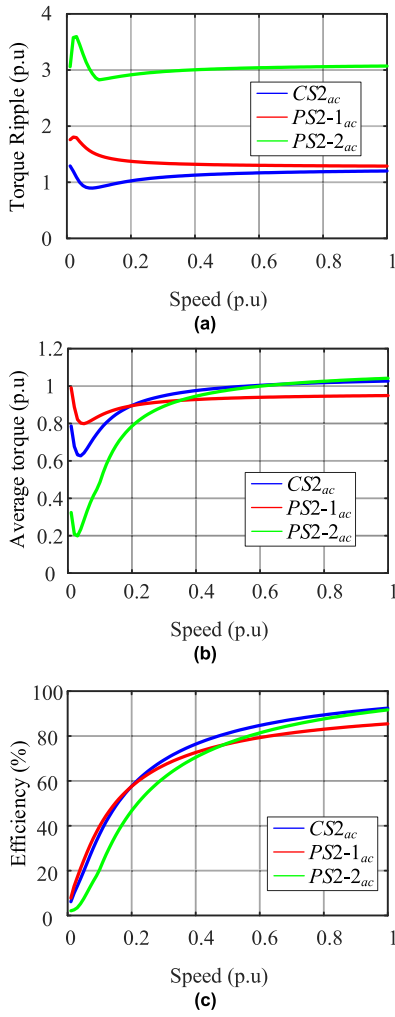
FIGURE 14. Characteristic curves for $CS2_{ac}$ strategy, $PS2\text{-}1_{ac}$ strategy and $PS2\text{-}2_{ac}$ strategy with third harmonic injection. (a) Torque ripple, (b) Average torque, (c) Efficiency.
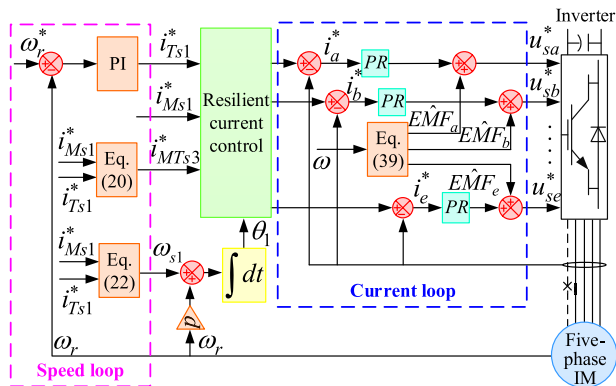

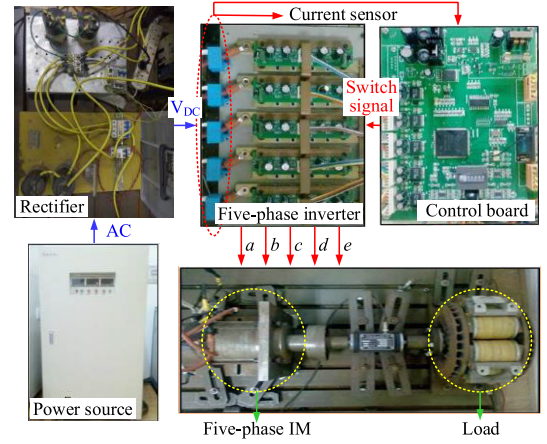**FIGURE 15.** Control structure for five-phase IM drive.
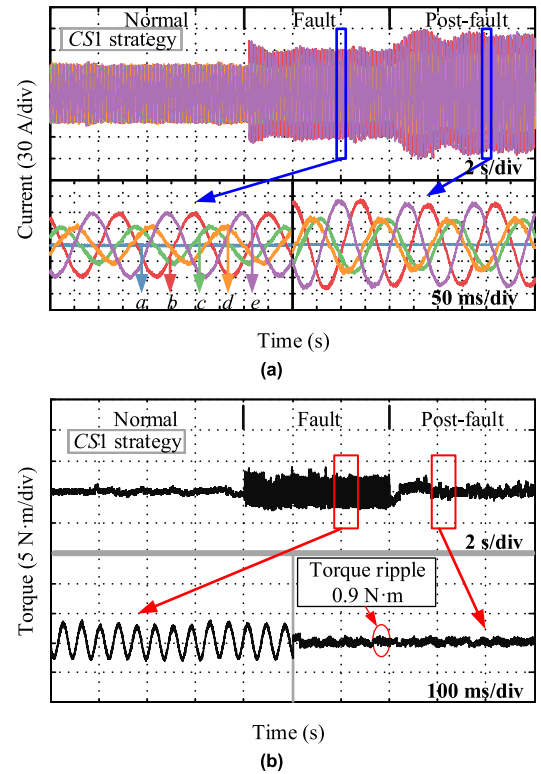

FIGURE 16. Experimental platform.

FIGURE 17. Currents and torque produced by $CS1$ under fundamental power supply. (a) Stator currents, (b) Measured torque.

Then the integral time constant τ_i is

$$\tau_i \approx \frac{10}{\omega_{c(\max)}} \quad (38)$$

By setting the open loop gain to unity and k_p is given as

$$k_p = \frac{R_s \tau_i}{V_{dc}} \omega_{c(\max)} \sqrt{\frac{1 + \omega_{c(\max)}^2 T_p^2}{1 + \omega_{c(\max)}^2 \tau_i^2}} \quad (39)$$

where $T_p = (l_{s1} + \frac{l_{r1} L_{m1}}{l_{r1}+L_{m1}})/R_s$. According to the mathematical analysis, the controller gains ($k_p = 0.5$ and
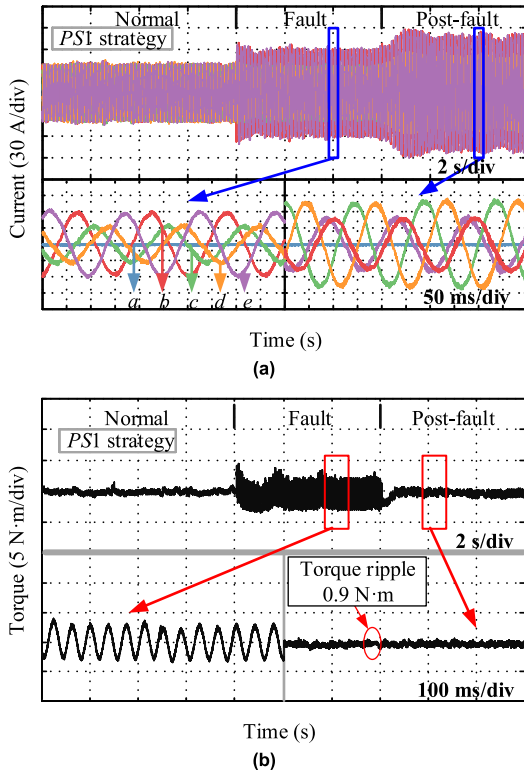
ω and 3ω [38]. The maximum cross frequency is

$$\omega_{c(\max)} = \frac{\pi/2 - \psi_m}{T_d} \quad (37)$$

FIGURE 18. Currents and torque produced by *PS*1 under fundamental power supply. (a) Stator currents, (b) Measured torque.
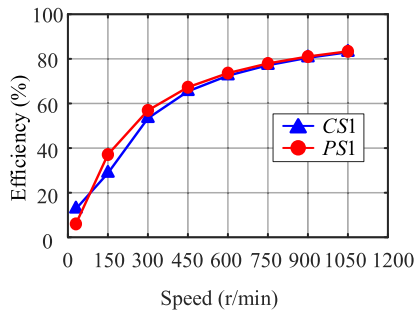

FIGURE 19. Efficiency comparison between *CS*1 and *PS*1 under fundamental power supply.

$\tau_i = 0.0019$) are applied in the current controller. In addition, the fundamental EMF is feedforward to compensate the current tracking error.

$$
\begin{cases}
E\hat{M}F_a = \dfrac{V_{rated}}{2\pi f_{rated}} \omega \cos(\omega t + \dfrac{\pi}{2}) \\[2mm]
E\hat{M}F_b = \dfrac{V_{rated}}{2\pi f_{rated}} \omega \cos(\omega t + \dfrac{\pi}{10}) \\[2mm]
E\hat{M}F_c = \dfrac{V_{rated}}{2\pi f_{rated}} \omega \cos(\omega t - \dfrac{3\pi}{10}) \\[2mm]
E\hat{M}F_d = \dfrac{V_{rated}}{2\pi f_{rated}} \omega \cos(\omega t - \dfrac{7\pi}{10}) \\[2mm]
E\hat{M}F_e = \dfrac{V_{rated}}{2\pi f_{rated}} \omega \cos(\omega t - \dfrac{11\pi}{10})
\end{cases}
\tag{40}
$$

FIGURE 20. Currents and torque produced by *CS*1 with third harmonic current injection. (a) Stator currents, (b) Measured torque.

FIGURE 21. Currents and torque produced by *PS*1 with third harmonic current injection. (a) Stator currents, (b) Measured torque.

V. EXPERIMENTAL RESULTS

The basic configuration of the experimental system is presented in Fig. 16. It consists of a five-phase IM interfaced with a digital control board using TMS320F28335. Coupled with

FIGURE 22. Efficiency comparison between *CS*1 and *PS*1 under third harmonic current injection.
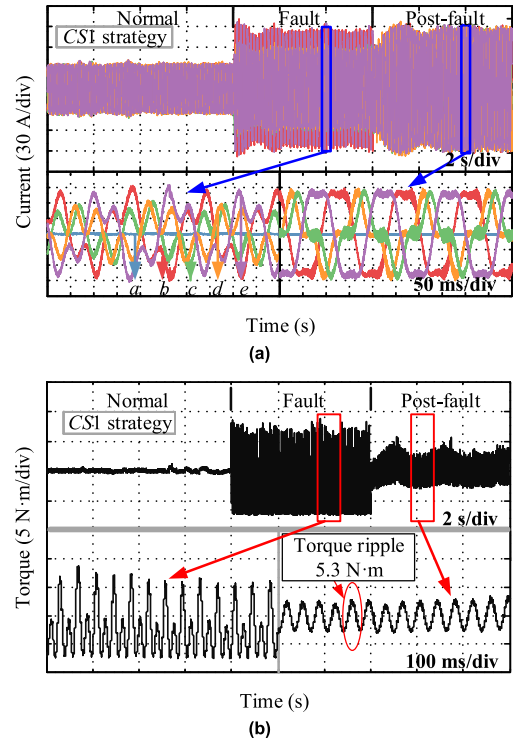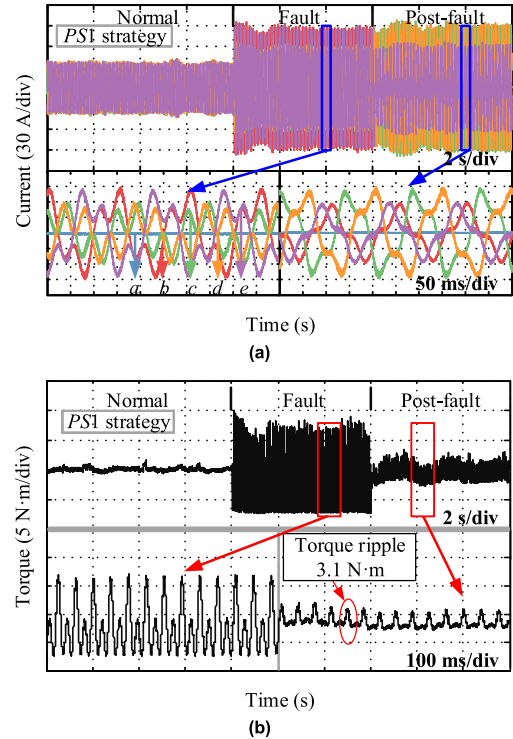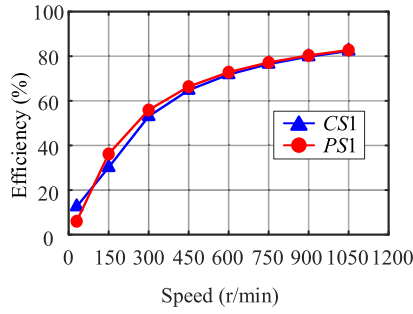

FIGURE 23. Currents and torque produced by *CS*2 with third harmonic current injection. (a) Stator currents, (b) Measured torque.
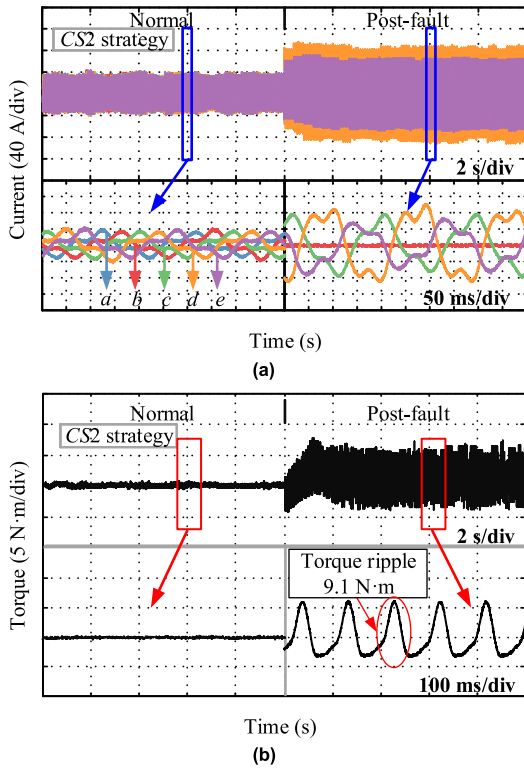

FIGURE 24. Currents and torque produced by *PS*2-1 with third harmonic current injection. (a) Stator currents, (b) Measured torque.

a vortex loader, the IM is driven by a five-phase voltage source inverter. The DC bus voltage is set for 72V, and the switching frequency is 10 kHz. The power device consists of four MOSFET with parallel structure for each phase. To evaluate the torque pulsations under different strategies, a torque observer in [32] is used by manipulating the current waveforms.

A. SINGLE-PHASE FAULT

According to the appendix, the amplitude of current commands of *CS*1 strategy and *PS*1 strategy are about 1.9 times larger than that in healthy condition, so the mechanical load is set to 10 N·m (about half load) in case the over-current occurs in the inverter module. The experimental results were
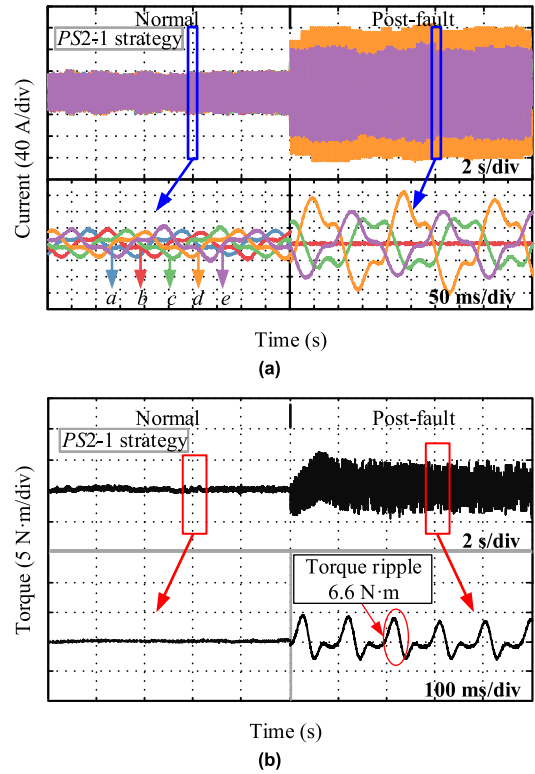
all obtained for the fault in phase "*a*" and the reference speed is set to 150 r/min. Fig. 17 and Fig. 18 shows the experimental results under fundamental power supply for *CS*1 strategy and *PS*1 strategy. The torque response and the stator currents contains normal operation, fault operation and post-fault operation. Fig. 17(b) and Fig. 18(b) show that *PS*1 strategy and *CS*1 strategy achieve almost the same torque ripple with the normal condition during post-fault operation, which is consistent with the theoretical results. The stator currents for *PS*1 and *CS*1 are depicted in Fig. 17(a) and Fig. 18(a). According to Fig. 19, *PS*1 achieve a higher efficiency than *CS*1 strategy from 150 r/min to 1050 r/min under fundamental power supply.

In the case of third harmonic supply, from Fig. 20(b) and Fig. 21(b), the torque ripple of *PS*1 strategy is smaller than *CS*1 strategy because the coupled SC $\overline{I_{31}}$ is removed. The stator currents are shown in Fig. 20(a) and Fig. 21(a). According to Fig. 22, *PS*1 achieve a higher efficiency than *CS*1 strategy from 150 r/min to 1050 r/min under fundamental power supply.

B. TWO-PHASE FAULT

According to the appendix, the amplitude of current commands of $CS2_{ab}$ strategy and $PS2\text{-}1_{ab}$ strategy are about 3.6 times larger than that in healthy condition, so the mechanical load is set to 5 N·m in case the over-current occurs in the inverter module. The experimental results were all obtained
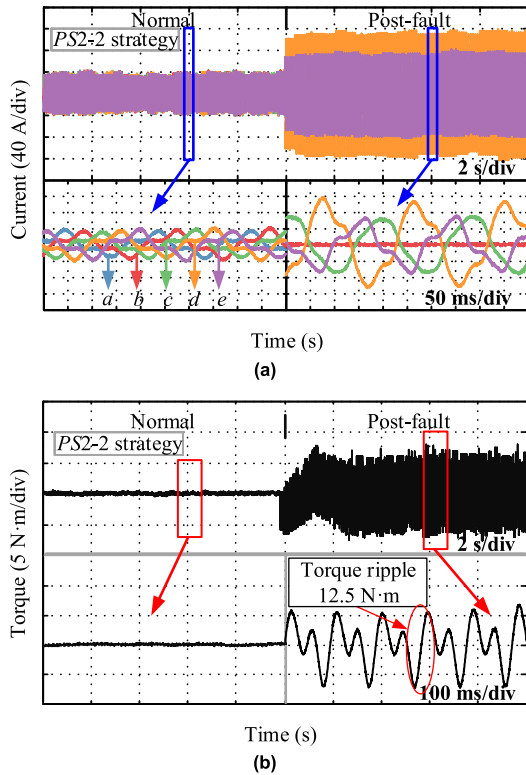
FIGURE 25. Currents and torque produced by *PS*2-2 with third harmonic current injection. (a) Stator currents, (b) Measured torque.
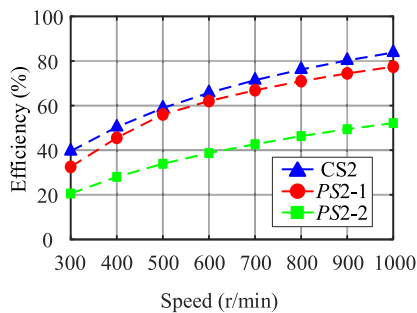

FIGURE 26. Efficiency comparison between *CS*2, *PS*2-1 and *PS*2-2 under third harmonic current injection.

FIGURE 27. Dynamic response by *PS*2-1$_{ab}$ with third harmonic current injection. (a) Stator currents, (b) Measured torque, (c) Speed.

*PS*2-2$_{ab}$ cannot be used because there is no improvement than *CS*2$_{ab}$ in terms of torque ripple and efficiency.

C. DYNAMIC PERFORMANCE

In order to test the dynamic performance of the proposed strategy, the *PS*2-1$_{ab}$ strategy under adjacent two-phase fault under is tested. With a load torque of 5 N·m under post-fault operation, the reference speed rises from 300 to 1000 r/min, and then decreases from 1000 to 300 r/min. The stator currents and torque response are shown in Fig. 27(a)-(b). According to Fig. 27(c), the speed is always stable during accelerating and decelerating process, which illustrates that the torque ripple can be minimized during dynamic process.

VI. CONCLUSION

Based on the MMF invariance, the conventional minimum torque ripple strategy suppresses the torque ripple by manipulate the MMF coupling. But the nonlinear analytical relationship between the torque ripple and MMF coupling is not considered, so the conventional strategy may not be the optimum solution. According to the steady-state model using SCs, ΔT_e^{14} plays a major role in the torque ripple and it is related to the first SC and fourth SC. Based on the MMF invariance, several current commands are proposed in this paper by suppressing the first SC and fourth SC. Single-phase fault and two-phase fault with third harmonic current injection are considered. Under single-phase fault, the proposed

for the fault in phase "*a*" and phase "*b*", and the reference speed is set to 300 r/min. Fig. 23-25 shows the experimental results under third harmonic current injection for *CS*2$_{ab}$ strategy, *PS*2-1$_{ab}$ strategy and *PS*2-2$_{ab}$ strategy. The torque response and the stator currents contains normal operation and post-fault operation. The *PS*2-1 strategy achieves the minimum torque ripple according to Fig. 23(a), Fig. 24(a) and Fig. 25(a), which is consistent with the simulation analysis. The stator currents for these three strategies are depicted in Fig. 23(b) and Fig. 24(b) and Fig. 25(b). According to Fig. 26, *PS*2-1$_{ab}$ achieves lower efficiency than *CS*2$_{ab}$ from 300 r/min to 1000 r/min under third harmonic injection.
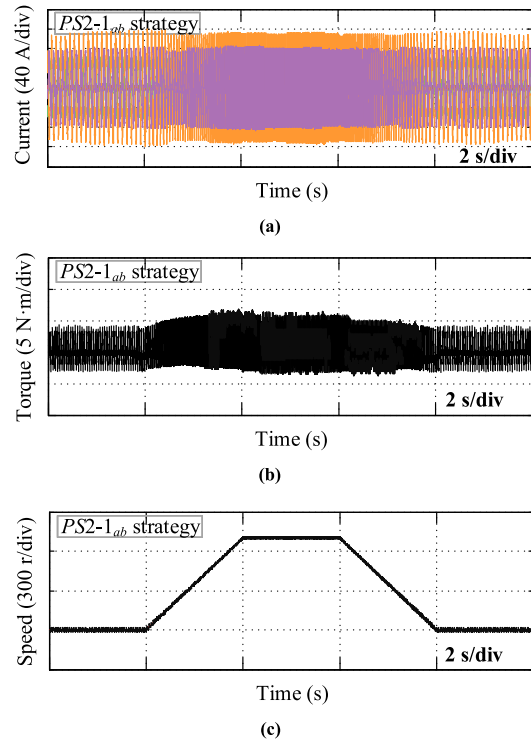
strategy (*PS*1) shows a better performance than the conventional strategy (*CS*1). Two strategies (*PS*2-1 and *PS*2-2) are proposed to optimize the third harmonic currents under two-phase fault. Under adjacent two-phase fault, *PS*2-1$_{ab}$ achieves the lowest torque ripple but with a lower efficiency than the conventional strategy (*CS*2$_{ab}$). In addition, *PS*2-2$_{ab}$ cannot be used because there is no improvement than *CS*2$_{ab}$ in terms of torque ripple and efficiency. Hence *PS*2-1$_{ab}$ and *CS*2$_{ab}$ can be selected according to the specific application requirements under adjacent two-phase fault. Under non-adjacent two-phase fault, it is better to use the conventional strategy (*CS*2$_{ac}$) and there are no performance improvements for *PS*2-1$_{ac}$ and *PS*2-2$_{ac}$.

APPENDIX

*CS*1

$$
\begin{cases}
i^*_{bCS1} = 1.902(i^*_{Ms1}\cos(\omega t - \tfrac{3\pi}{10}) + i^*_{Ts1}\sin(\omega t - \tfrac{3\pi}{10})) \\
\quad + 1.175(i^*_{Ms3}\cos 3(\omega t - \tfrac{3\pi}{10}) + i^*_{Ts3}\sin 3(\omega t - \tfrac{3\pi}{10})) \\
i^*_{cCS1} = 1.175(i^*_{Ts1}\cos(\omega t + \tfrac{9\pi}{10}) + i^*_{Ms1}\sin(\omega t + \tfrac{9\pi}{10})) \\
\quad + 1.902(i^*_{Ts3}\cos 3(\omega t - \tfrac{\pi}{10}) + i^*_{Ms3}\sin 3(\omega t - \tfrac{\pi}{10})) \\
i^*_{dCS1} = 1.175(i^*_{Ts1}\cos(\omega t - \tfrac{9\pi}{10}) + i^*_{Ms1}\sin(\omega t - \tfrac{9\pi}{10})) \\
\quad + 1.902(i^*_{Ts3}\cos 3(\omega t + \tfrac{\pi}{10}) + i^*_{Ms3}\sin 3(\omega t + \tfrac{\pi}{10})) \\
i^*_{eCS1} = 1.902(i^*_{Ts1}\cos(\omega t + \tfrac{3\pi}{10}) + i^*_{Ms1}\sin(\omega t + \tfrac{3\pi}{10})) \\
\quad + 1.175(i^*_{Ts3}\cos 3(\omega t + \tfrac{3\pi}{10}) + i^*_{Ms3}\sin 3(\omega t + \tfrac{3\pi}{10}))
\end{cases}
$$

(A.1)

*PS*1

$$
\begin{cases}
i^*_{bPS1} = 1.175(i^*_{Ts1}\cos(\omega t - \tfrac{\pi}{10}) + i^*_{Ms1}\sin(\omega t - \tfrac{\pi}{10})) \\
\quad + 1.175(i^*_{Ts3}\cos 3(\omega t + \tfrac{\pi}{6}) + i^*_{Ms3}\sin 3(\omega t + \tfrac{\pi}{6})) \\
i^*_{cPS1} = 1.902(i^*_{Ts1}\cos(\omega t - \tfrac{7\pi}{10}) + i^*_{Ms1}\sin(\omega t - \tfrac{7\pi}{10})) \\
\quad + 1.902(i^*_{Ts3}\cos 3(\omega t - \tfrac{\pi}{6}) + i^*_{Ms3}\sin 3(\omega t - \tfrac{\pi}{6})) \\
i^*_{dPS1} = 1.902(i^*_{Ts1}\cos(\omega t + \tfrac{7\pi}{10}) + i^*_{Ms1}\sin(\omega t + \tfrac{7\pi}{10})) \\
\quad + 1.902(i^*_{Ts3}\cos 3(\omega t + \tfrac{\pi}{6}) + i^*_{Ms3}\sin 3(\omega t + \tfrac{\pi}{6})) \\
i^*_{ePS1} = 1.175(i^*_{Ts1}\cos(\omega t + \tfrac{\pi}{10}) + i^*_{Ms1}\sin(\omega t + \tfrac{\pi}{10})) \\
\quad + 1.175(i^*_{Ts3}\cos 3(\omega t - \tfrac{\pi}{6}) + i^*_{Ms3}\sin 3(\omega t - \tfrac{\pi}{6}))
\end{cases}
$$

(A.2)

*CS*2$_{ab}$

$$
\begin{cases}
i^*_{cCS2} = 2.236(i^*_{Ts1}\cos(\omega t - \tfrac{2\pi}{5}) + i^*_{Ms1}\sin(\omega t - \tfrac{2\pi}{5})) \\
\quad + 2.236(i^*_{Ts3}\cos 3(\omega t - \tfrac{2\pi}{15}) + i^*_{Ms3}\sin 3(\omega t - \tfrac{2\pi}{15})) \\
i^*_{dCS2} = 3.618(i^*_{Ts1}\cos(\omega t + \tfrac{4\pi}{5}) + i^*_{Ms1}\sin(\omega t + \tfrac{4\pi}{5})) \\
\quad + 3.618(i^*_{Ts3}\cos 3(\omega t + \tfrac{4\pi}{15}) + i^*_{Ms3}\sin 3(\omega t + \tfrac{4\pi}{15})) \\
i^*_{eCS2} = 2.236(i^*_{Ts1}\cos(\omega t) + i^*_{Ms1}\sin(\omega t)) \\
\quad + 2.236(i^*_{Ts3}\cos 3\omega t + i^*_{Ms3}\sin 3\omega t)
\end{cases}
$$

(A.3)

*PS*2 − 1$_{ab}$

$$
\begin{cases}
i^*_{cPS2-1} = 2.236(i^*_{Ts1}\cos(\omega t - \tfrac{2\pi}{5}) + i^*_{Ms1}\sin(\omega t - \tfrac{2\pi}{5})) \\
\quad + 2.236(i^*_{Ts3}\cos 3(\omega t - \tfrac{4\pi}{15}) + i^*_{Ms3}\sin 3(\omega t - \tfrac{4\pi}{15})) \\
i^*_{dPS2-1} = 3.618(i^*_{Ts1}\cos(\omega t + \tfrac{4\pi}{5}) + i^*_{Ms1}\sin(\omega t + \tfrac{4\pi}{5})) \\
\quad + 3.618(i^*_{Ts3}\cos 3(\omega t + \tfrac{2\pi}{15}) + i^*_{Ms3}\sin 3(\omega t + \tfrac{2\pi}{15})) \\
i^*_{ePS2-1} = 2.236(i^*_{Ts1}\cos(\omega t) + i^*_{Ms1}\sin(\omega t)) \\
\quad + 2.236(i^*_{Ts3}\cos 3(\omega t - \tfrac{2\pi}{15}) + i^*_{Ms3}\sin 3(\omega t - \tfrac{2\pi}{15}))
\end{cases}
$$

(A.4)

*PS*2 − 2$_{ab}$

$$
\begin{cases}
i^*_{cPS2-2} = 2.236(i^*_{Ts1}\cos(\omega t - \tfrac{2\pi}{5}) + i^*_{Ms1}\sin(\omega t - \tfrac{2\pi}{5})) \\
\quad + 1.382(i^*_{Ts3}\cos 3(\omega t - \tfrac{2\pi}{15}) + i^*_{Ms3}\sin 3(\omega t - \tfrac{2\pi}{15})) \\
i^*_{dPS2-2} = 3.618(i^*_{Ts1}\cos(\omega t + \tfrac{4\pi}{5}) + i^*_{Ms1}\sin(\omega t + \tfrac{4\pi}{5})) \\
\quad + 2.236(i^*_{Ts3}\cos 3(\omega t + \tfrac{2\pi}{15}) + i^*_{Ms3}\sin 3(\omega t + \tfrac{2\pi}{15})) \\
i^*_{ePS2-2} = 2.236(i^*_{Ts1}\cos(\omega t) + i^*_{Ms1}\sin(\omega t)) \\
\quad + 1.382(i^*_{Ts3}\cos 3(\omega t - \tfrac{4\pi}{15}) + i^*_{Ms3}\sin 3(\omega t - \tfrac{4\pi}{15}))
\end{cases}
$$

(A.5)

REFERENCES

[1] E. Levi, "Multiphase electric machines for variable-speed applications," *IEEE Trans. Ind. Electron.*, vol. 55, no. 5, pp. 1893–1909, May 2008.

[2] T. S. de Souza, R. R. Bastos, and B. J. C. Filho, "Modeling and control of a nine-phase induction machine with open phases," *IEEE Trans. Ind. Appl.*, vol. 54, no. 6, pp. 6576–6585, Nov. 2018.

[3] E. Jung, H. Yoo, S.-K. Sul, H.-S. Choi, and Y.-Y. Choi, "A nine-phase permanent-magnet motor drive system for an ultrahigh-speed elevator," *IEEE Trans. Ind. Appl.*, vol. 48, no. 3, pp. 987–995, May/Jun. 2012.

[4] Z. Liu, J. Wu, and L. Hao, "Coordinated and fault-tolerant control of tandem 15-phase induction motors in ship propulsion system," *IET Electr. Power Appl.*, vol. 12, no. 1, pp. 91–97, Jan. 2018.

[5] M. J. Duran and F. Barrero, "Recent advances in the design, modeling, and control of multiphase machines—Part II," *IEEE Trans. Ind. Electron.*, vol. 63, no. 1, pp. 459–468, Jan. 2016.
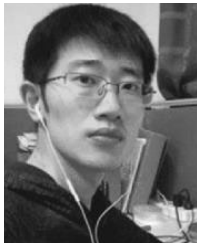
[6] J. Liu, L. Huang, H. Yu, C. Wen, and W. Zhong, "Study on the characteristics of a novel six-phase fault-tolerant linear permanent magnet machine for linear oil pumping," *IEEE Trans. Appl. Supercond.*, vol. 24, no. 3, pp. 1–5, Jun. 2014.

[7] H. Guzman, M. J. Duran, F. Barrero, B. Bogado, and S. Toral, "Speed control of five-phase induction motors with integrated open-phase fault operation using model-based predictive current control techniques," *IEEE Trans. Ind. Electron.*, vol. 61, no. 9, pp. 4474–4484, Sep. 2014.

[8] M. Bermudez, I. G. Prieto, F. Barrero, H. Guzman, M. J. Duran, and X. Kestelyn, "Open-phase fault-tolerant direct torque control technique for five-phase induction motor drives," *IEEE Trans. Ind. Electron.*, vol. 64, no. 2, pp. 902–911, Feb. 2017.

[9] A. S. Abdel-Khalik, M. S. Hamad, A. M. Massoud, and S. Ahmed, "Post-fault operation of a nine-phase six-terminal induction machine under single open-line fault," *IEEE Trans. Ind. Electron.*, vol. 65, no. 2, pp. 1084–1096, Feb. 2018.

[10] W. Cao, B. C. Mecrow, G. J. Atkinson, J. W. Bennett, and D. J. Atkinson, "Overview of electric motor technologies used for more electric aircraft (MEA)," *IEEE Trans. Ind. Electron.*, vol. 59, no. 9, pp. 3523–3531, Sep. 2012.

[11] Z. Liu, Z. Zheng, and Y. Li, "Enhancing fault-tolerant ability of a nine-phase induction motor drive system using fuzzy logic current controllers," *IEEE Trans. Energy Convers.*, vol. 32, no. 2, pp. 759–769, Jun. 2017.

[12] Y. Zhao and T. A. Lipo, "Modeling and control of a multi-phase induction machine with structural unbalance, Part I: Machine modeling and multi-dimensional current regulation," *IEEE Trans. Energy Convers.*, vol. 11, no. 3, pp. 570–577, Sep. 1996.

[13] Y. Zhao and T. A. Lipo, "Modeling and control of a multi-phase induction machine with structural unbalance, Part II: Field-oriented control and experimental verification," *IEEE Trans. Energy Convers.*, vol. 11, no. 3, pp. 570–577, Sep. 1996.

[14] R. Kianinezhad, B. Nahid-Mobarakeh, L. Baghli, F. Betin, and G.-A. Capolino, "Modeling and control of six-phase symmetrical induction machine under fault condition due to open phases," *IEEE Trans. Ind. Electron.*, vol. 55, no. 5, pp. 1966–1977, May 2008.

[15] P. Zhu, X. Zhang, M. Qiao, W. Cai, and J. Liang, "A novel control strategy for five-phase concentrated full-pitch windings induction motor under open-phase fault," in *Proc. Int. Conf. Machatronics Autom.*, 2011, pp. 950–955.

[16] H. Liu, D. Wang, X. Yi, and F. Meng, "Torque ripple suppression under open-phase fault conditions in a five-phase induction motor with harmonic injection," *IEEE Trans. Emerg. Sel. Topics Power Electron.*, early access, Nov. 2019, doi: 10.1109/JESTPE.2019.2952374.

[17] S. He, X. Sui, and F. Blaabjerg, "Comparative study of different fault tolerant control strategies for a five-phase concentrated-full-pitch winding induction motor," in *Proc. 21st Eur. Conf. Power. Electron. Appl.*, 2019, pp. P.1–P.10.

[18] H. Xu, H. A. Toliyat, and L. J. Petersen, "Resilient current control of five-phase induction motor under asymmetrical fault conditions," in *Proc. IEEE 17th Appl. Power Electron. Conf. Expo.*, Mar. 2002, pp. 64–71.

[19] H. S. Che, M. J. Duran, E. Levi, M. Jones, W.-P. Hew, and N. A. Rahim, "Postfault operation of an asymmetrical six-phase induction machine with single and two isolated neutral points," *IEEE Trans. Power Electron.*, vol. 29, no. 10, pp. 5406–5416, Oct. 2014.

[20] L. Zheng, J. E. Fletchert, and B. W. Williams, "Current optimization for a multi-phase machine under an open circuit phase fault condition," in *Proc. IET 3rd Int. Conf. Power Electron., Mach. Drives*, 2006, pp. 414–419.

[21] M. Kang, J. Huang, J. Yang, D. Liu, and H. Jiang, "Strategies for the fault-tolerant current control of a multiphase machine under open phase conditions," in *Proc. Int. Conf. Electr. Mach. Syst.*, 2009, pp. 1–6.

[22] A. Ashoush, S. M. Gadoue, A. S. Abdel-Khalik, and A. L. Mohamadein, "Current optimization for an eleven-phase induction machine under fault conditions using genetic algorithm," in *Proc. IEEE Int. Symp. Diagnostics Elect. Mach. Power Electron. Drives*, Sep. 2011, pp. 529–534.

[23] S. He, J. Huang, and M. Kang, "Post-fault operation for five-phase induction machines under single-phase open using symmetrical components," in *Proc. IEEE 32nd Appl. Power Electron. Conf. Expo.*, Mar. 2018, pp. 218–222.

[24] A. Tani, M. Mengoni, L. Zarri, G. Serra, and D. Casadei, "Control of multiphase induction motors with an odd number of phases under open-circuit phase faults," *IEEE Trans. Power Electron.*, vol. 27, no. 2, pp. 565–577, Feb. 2012.

[25] W. Kong, M. Kang, D. Li, R. Qu, D. Jiang, and C. Gan, "Investigation of spatial harmonic magnetic field coupling effect on torque ripple for multiphase induction motor under open fault condition," *IEEE Trans. Power Electron.*, vol. 33, no. 7, pp. 6060–6071, Jul. 2018.

[26] H. Lee and Y. Choi, "A new actuator system using dual-motors and a planetary gear," *IEEE/ASME Trans. Mechatronics*, vol. 17, no. 1, pp. 192–197, Feb. 2012.

[27] P. Hamelin, P. Bigras, J. Beaudry, P.-L. Richard, and M. Blain, "Discrete-time state feedback with velocity estimation using a dual observer: Application to an underwater direct-drive grinding robot," *IEEE/ASME Trans. Mechatronics*, vol. 17, no. 1, pp. 187–191, Feb. 2012.

[28] A. S. Abdel-Khalik, M. I. Masoud, and B. W. Williams, "Improved flux pattern with third harmonic injection for multiphase induction machines," *IEEE Trans. Power Electron.*, vol. 27, no. 3, pp. 1563–1578, Mar. 2012.

[29] S. He, J. Huang, and M. Kang, "A novel third harmonic current injection method to optimize the air-gap flux for multiphase induction machine," in *Proc. Int. Conf. Electr. Mach. Syst.*, 2017, pp. 1–6.

[30] W. Kong, J. Huang, R. Qu, M. Kang, and J. Yang, "Nonsinusoidal power supply analysis for concentrated-full-pitch-winding multiphase induction motor," *IEEE Trans. Ind. Electron.*, vol. 63, no. 1, pp. 574–582, Jan. 2016.

[31] C. L. Fortescue, "Method of symmetrical co-ordinates applied to the solution of polyphase networks," *Trans. Amer. Inst. Electr. Eng.*, vol. 37, no. 2, pp. 1027–1140, Jul. 1918.

[32] A. S. Abdel-Khalik, A. S. Morsy, S. Ahmed, and A. M. Massoud, "Effect of stator winding connection on performance of five-phase induction machines," *IEEE Trans. Ind. Electron.*, vol. 61, no. 1, pp. 3–19, Jan. 2014.

[33] A. Samy Abdel-Khalik, S. Ahmed, and A. M. Massoud, "Steady-state equivalent circuit of five-phase induction machines with different stator connections under open-line conditions," *IEEE Trans. Ind. Electron.*, vol. 63, no. 8, pp. 4651–4662, Aug. 2016.

[34] A. Arafat, S. Choi, and J. Baek, "Open-phase fault detection of a five-phase permanent magnet assisted synchronous reluctance motor based on symmetrical components theory," *IEEE Trans. Ind. Electron.*, vol. 64, no. 8, pp. 6465–6474, Aug. 2017.

[35] Z. Liu, Z. Zheng, L. Xu, K. Wang, and Y. Li, "Current balance control for symmetrical multiphase inverters," *IEEE Trans. Power Electron.*, vol. 31, no. 6, pp. 4005–4012, Jun. 2016.

[36] Z. Liu, Z. Zheng, Q. Wang, and Y. Li, "Enhanced rotor field-oriented control of multiphase induction machines based on symmetrical components theory," *IET Power Electron.*, vol. 12, no. 4, pp. 656–666, Apr. 2019.

[37] M. Schubert, S. Koschik, and R. W. De Doncker, "Fast optimal efficiency flux control for induction motor drives in electric vehicles considering core losses, main flux saturation and rotor deep bar effect," in *Proc. IEEE 28th Appl. Power Electron. Conf. Expo.*, Mar. 2013, pp. 811–816.

[38] D. G. Holmes, T. A. Lipo, B. P. McGrath, and W. Y. Kong, "Optimized design of stationary frame three phase AC current regulators," *IEEE Trans. Power Electron.*, vol. 24, no. 11, pp. 2417–2426, Nov. 2009.

SHAN HE (Graduate Student Member, IEEE) received the B.Eng. degree in electrical engineering from Northeast Electric Power University, Jilin, China, in 2015, and the M.Sc. degree in electrical engineering from Zhejiang University, Hangzhou, China, in 2018. He is currently pursuing the Ph.D. degree in electrical engineering with Aalborg University, Aalborg, Denmark. His research interests include multiphase induction motor and grid-connected inverter.

XIN SUI (Graduate Student Member, IEEE) received the B.Eng. degree in electrical engineering from Northeast Electric Power University, Jilin, China, in 2015, and the M.Sc. degree in electrical engineering from the Institute of Electrical Engineering, Chinese Academy of Sciences, Beijing, China, in 2018. She is currently pursuing the Ph.D. degree in electrical engineering with Aalborg University, Aalborg, Denmark. Her research interest includes battery health management.

ZIJIAN LIU received the B.S. degree from the Huazhong University of Science and Technology, Wuhan, China, in 2012, the M.S. degree in electrical engineering from the Harbin Institute of Technology, Harbin, in 2014, and the Ph.D. degree in electrical engineering from Zhejiang University, Hangzhou, China, in 2018. Since 2018, he has been with the Department of Electric Engineering, Tsinghua University, Beijing, China, where he is curr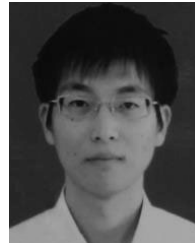ently a Postdoctoral Researcher. His current research interests include design and control of the interior permanent magnet synchronous motor, condition monitoring, and fault diagnosis of AC machines.

MIN KANG received the B.S. and Ph.D. degrees from the College of Electrical Engineering, Zhejiang University, Hangzhou, China, in 2003 and 2008, respectively.

From 2008 to 2011, he was a Lecturer with the College of Electrical Engineering, Zhejiang University of Science and Technology, China. He is currently a Professor with the Zhejiang University of Science and Technology. His research interests include multiphase machines and AC drives.

DAO ZHOU (Senior Member, IEEE) received the B.S. degree in electrical engineering from Beijing Jiaotong University, Beijing, China, in 2007, the M.S. degree in power electronics from Zhejiang University, Hangzhou, China, in 2010, and the Ph.D. degree from Aalborg University, Aalborg, Denmark, in 2014. Since 2014, he has been with the Department of Energy Technology, Aalborg University, where he is currently an Assistant Professor. His research interests include modeling, control, and reliability of power electronics in renewable energy application.

FREDE BLAABJERG (Fellow, IEEE) received the Ph.D. degree in electrical engineering from Aalborg University, in 1995, and the Honoris Causa degree from the University Politehnica Timisoara (UPT), Romania, and Tallinn Technical University (TTU), Estonia.

From 1987 to 1988, he was with ABB-Scandia, Randers, Denmark. He was an Assistant Professor, an Associate Professor, and a Full Professor of power electronics and drives with Aalborg University, in 1992, 1996, and 1998, respectively, where he has been a Villum Investigator, since 2017. He has published more than 600 journal articles in the fields of power electronics and its applications. He has coauthored four monographs. His current research interests include power electronics and its applications, such as wind turbines, PV systems, reliability, harmonics, and adjustable speed drives. He is an Editor of ten books in power electronics and its applications.

• • •